

## Phase Stability and Magnetism of Ternary Laves Phases

Alexander Kerkau, Manuel Brando, and Guido Kreiner

The modeling of phase formation and crystal structures is still a major challenge in solid-state chemistry [1–3]. A crystal structure may sometimes be guessed based on information from the chemical composition, the crystal structure of a neighboring phase and by applying chemical bonding concepts. However, only first-principles calculations effectively allow to model phase formation, crystal structures and disorder phenomena.

Recently, we have been able to model the phenomenon of preferential site occupation [4] for the ternary C14 Laves phase  $\text{Nb}(\text{Cr}_{1-x}\text{Co}_x)_2$ , which is formed in a large homogeneity range from  $0.127(3) \leq x \leq 0.937(3)$  at  $1100^\circ\text{C}$ . The ansatz is based on the idea of computing the partition function  $Z_N$  for the Laves phase  $\text{Nb}(\text{Cr}_{1-x}\text{Co}_x)_2$  using the ordered superstructures of  $\text{Nb}_4\text{Cr}_{8-N}\text{Co}_N$  as an approximation. For a given  $N$  between 2 and 6, one has to consider all possible ways of distributing these  $N$  Co atoms among the crystallographic sites  $2a$  and  $6h$ . If  $E$  denotes the total energy,  $p$  the number of Co atoms occupying the  $2a$  site,  $M$  the number of symmetrically inequivalent configurations and  $g$  the multiplicity, then  $Z_N$  is given by:

$$Z_N = \sum_{\sigma=1}^M g_{N,p;\sigma} \exp(-E_{N,p;\sigma} / (k_B T)) \quad (1)$$

In this case, the calculation predicts a preferential site occupation of the respective minority component on the  $2a$  site and a site occupation reversal at approximately  $x = 0.5$ . The computed values are in good agreement with the experimental data.

Since it was possible to model the short range order in a ternary C14 Laves phase we have extended the computations to calculate the unit cell volume, the lattice parameters, the  $c/a$  ratio and the phase stability of C15 and C14 phases along quasi-binary sections  $AB_2-AB'_2$ . The computed properties are suitable for multiple uses: (i) they help to minimize the number of required experiments along the section  $AB_2-AB'_2$  because the computation predicts the general curve shape; (ii) in the case of the absolute values deviating from the experiment, the calculated values can be calibrated

by a small number of experimental data; (iii) a system can be probed for unexpected behavior.

### Cell Geometry of $\text{Nb}(\text{Cr}_{1-x}\text{Co}_x)_2$

The lattice parameters  $a$  and  $c$ , the mean atomic volume and the  $c/a$  ratio have been calculated using the partition function in the same way as the site occupation factors. However, a supercell has been used to increase the number of compositional data points. First-principles total-energy calculations were performed with the Vienna Ab-Initio Simulation Package (VASP) [5] within the generalized gradient approximation (GGA) [6]. The calculated data as shown in Figure 1 are based on a  $2 \times 1 \times 1$  supercell, i.e.,  $\text{Nb}_8\text{Cr}_{16-N}\text{Co}_N$  with  $N = 1-16$ .

The calculated unit cell parameters are slightly smaller than the experimental data. The experimental and the calculated data for the mean atomic volume follow Vegard's volume rule. Both data sets can be brought into conformance by adding the volume difference from one data point to the experimental data. The curve shape of the  $c/a$  ratio for C14  $\text{Nb}(\text{Cr}_{1-x}\text{Co}_x)_2$  can be described by an S-type behavior with the inflection point at  $x \approx 0.6$  and the minimum at  $x \approx 0.8$ . The absolute values of the cal-

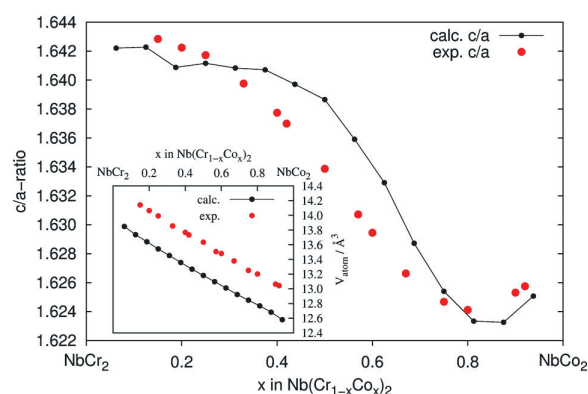


Fig. 1: Experimental and calculated  $c/a$  ratio for C14  $\text{Nb}(\text{Cr}_{1-x}\text{Co}_x)_2$ . The calculated data are temperature scaled by using the experimental  $c/a$  ratio at the predicted minimum. The inset shows the calculated and the experimental mean atomic volume. The calculated data are not fitted to the experimental for reasons of clarity.

culated  $c/a$  ratio differ from the experimentally obtained values. However, the general S-shape, the location of the inflection point and the minimum and maximum are well captured. The calculated  $c/a$  ratio curve can be fitted to the experimental values by changing the temperature  $T$  in Eq. 1 using the  $c/a$  ratio at the predicted minimum.

### Phase Stability of $\text{Nb}(\text{Cr}_{1-x}\text{Co}_x)_2$ and $\text{Ta}(\text{V}_{1-x}\text{Fe}_x)_2$

In order to determine the composition dependent stability of the C14 and the C15 structure type along the section  $\text{NbCr}_2\text{--NbCo}_2$ , the Gibbs energy  $\Delta G$  has been calculated. For cubic C15,  $\text{Nb}_8\text{Cr}_{16-N}\text{Co}_N$  was chosen as a model system. For each  $N$  between 0 and 16, we have considered all possible ways of distributing the  $N$  Co atoms among the  $16c$  site of the unit cell. First-principles total-energy calculations were then performed only for the symmetrically inequivalent configurations. In a similar way, we calculated the total-energies for C14  $\text{Nb}(\text{Cr}_{1-x}\text{Co}_x)_2$  based on  $\text{Nb}_8\text{Cr}_{16-N}\text{Co}_N$ . The same unit cell content as for the C15 phase was obtained by using  $2 \times 1 \times 1$  supercells. The  $N$  Co atoms were distributed among the  $2a$  and  $6h$  sites of the hexagonal unit cell.

The Gibbs energy  $\Delta G$  is given by:

$$\Delta G = \Delta H - T\Delta S \quad (2)$$

The entropy for C15 and C14  $\text{Nb}(\text{Cr}_{1-x}\text{Co}_x)_2$  as disordered solution phases employing the ideal solution model is given by:

$$\Delta S = -R[x \cdot \ln(x) + (1-x) \cdot \ln(1-x)] \quad (3)$$

The heat of formation  $\Delta H$  was then calculated for the configuration with the lowest energy at each point  $N$  from the total-energy of the compounds and the total-energy of the elements Nb, Cr and Co:

$$\Delta H = E_{\text{Nb}(\text{Cr}_{1-x}\text{Co}_x)_2} - E_{\text{Nb}} - (2-2x) \cdot E_{\text{Cr}} - 2x \cdot E_{\text{Co}} \quad (4)$$

The Gibbs energy of the stable configurations of the C15 and the C14 structure at the composition  $N/16$  with  $N = 0\text{--}16$  are shown in Figure 2. The values are fitted with Redlich-Kister polynomials of 4<sup>th</sup> order:

$$\Delta G = ((x-1) \cdot \Delta G_{AB_2} + x \cdot \Delta G_{AB'_2}) + (x-x^2) \cdot [{}^0A + {}^1A(2x-1) + {}^2A(2x-1)^2 + {}^3A(2x-1)^3 + {}^4A(2x-1)^4] \quad (5)$$

The phase boundaries associated with the first-order transition between the phases with C15 and C14 structure were located using the tangent construction.

The calculations predict in agreement with the experiment that  $\text{NbCr}_2$  and  $\text{NbCo}_2$  crystallize with the cubic C15 structure type. A small solubility of 2 at.% Co in C15  $\text{NbCr}_2$  is expected followed by a two-phase field up to 12 at.% Co. Due to the limited number of data points, the location of the two-phase field C14/C15 on the Co-rich side cannot be determined by the tangent construction. However, a small solubility for Cr in C15  $\text{NbCo}_2$  is expected from the data and a C14 phase  $\text{Nb}(\text{Cr}_{1-x}\text{Co}_x)_2$  should form with a broad homogeneity range. The predictions are in good agreement with the experimental data as indicated by the top and bottom bars in Figure 2.

As a second example, the system  $\text{TaV}_2\text{--TaFe}_2$  has been chosen to compare calculated with experimental data. No information for this system is available in the literature, except that  $\text{TaV}_2$  and  $\text{TaFe}_2$  crystallize with the C15 [7] and the C14 structure type [8], respectively.  $\text{TaFe}_2$  is a paramagnet very close to a magnetic instability with strong ferromagnetic (FM) and antiferromagnetic (AFM) spin fluctuations [9]. Hence, one can expect that spin polarization plays an important role.

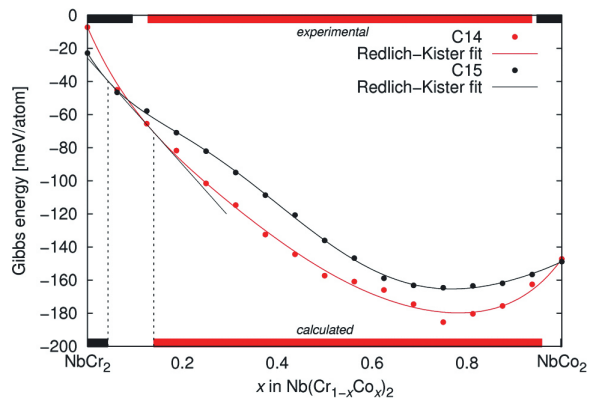


Fig. 2: Gibbs energy of C15 and C14  $\text{Nb}(\text{Cr}_{1-x}\text{Co}_x)_2$ . The solid lines are fits with Redlich-Kister polynomials. The top and bottom bars indicate the experimentally determined and the calculated width of the single phase fields of C15 and C14, respectively.

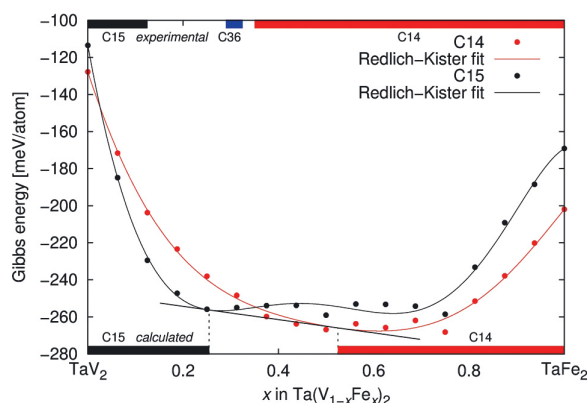


Fig. 3: Gibbs energy of C15 and C14  $\text{Ta}(\text{V}_{1-x}\text{Fe}_x)_2$ . The solid lines are fits with Redlich-Kister polynomials. The bottom bars indicate the width of the single phase fields of C15 and C14.

However, due to the large number of structural/magnetic configurations spin polarization was not included in the current calculations.

The Gibbs energy of the stable configurations of the C15 and C14 phases are shown in Figure 3. The calculation predicts a solubility of Fe in  $\text{TaV}_2$  up to 24 at.% and of V in C14  $\text{TaFe}_2$  up to 39 at.%. An additional phase change from C15 to C14 close to  $\text{TaV}_2$  and the stability of C14  $\text{TaV}_2$  is expected from the calculated data. However, this is inconsistent with the experimental results. It is known that pseudo potential calculations tend to make wrong predictions in the case of Laves phases containing V [10]. If a full-potential code like FPLO is used [11], C15  $\text{TaV}_2$  is the stable polytype, in agreement with the experiments.

A series of  $\text{Ta}(\text{V}_{1-x}\text{Fe}_x)_2$  alloys with various Fe and V contents was prepared by arc-melting high purity elements as starting materials and performing a subsequent heat treatment at 1150 °C for 30 days. After the annealing, the samples were quenched in water. The composition of the samples was determined with ICP-OES. Metallographic examinations were carried out to check the phase content. The maximal solubility of Fe in  $\text{TaV}_2$  at 1150 °C is 8 at.%, while the solubility of V in  $\text{TaFe}_2$  is 43 at.%. In addition, a ternary Laves phase of the hexagonal C36 type has been observed with a small homogeneity range of  $0.29 \leq x \leq 0.32$ . Figure 4 shows the experimental results of the phase analysis and the mean atomic volume plotted versus the composition  $x$ . As expected, the mean atomic volume decreases with increasing Fe content and the volume behaves according to Vegard's volume rule.

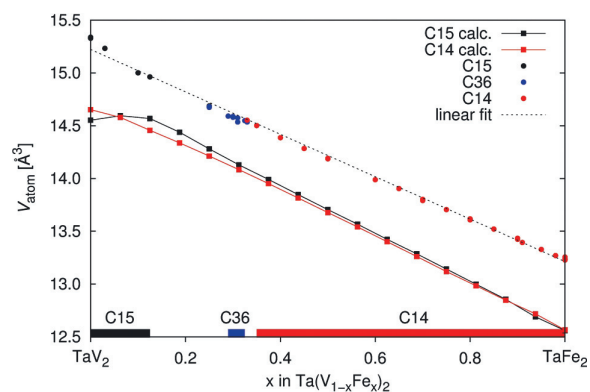


Fig. 4: Experimental and calculated mean atomic volume  $V_{\text{atom}}$  of  $\text{Ta}(\text{V}_{1-x}\text{Fe}_x)_2$  against the composition  $x$ . The bottom bars indicate the experimentally determined width of the single phase fields of C15, C36 and C14.

The calculated values are in good agreement with the experimental data, after the volume correction, except for the C15 phase close to  $\text{TaV}_2$ . The reasons for the deviation of the calculated mean atomic volume close to  $\text{TaV}_2$  are yet unclear, but can be related to the wrongly predicted stability of C14  $\text{TaV}_2$ .

### Magnetism of $\text{Ta}(\text{V}_{1-x}\text{Fe}_x)_2$

The change of the crystal structure is not the only interesting issue in  $\text{Ta}(\text{V}_{1-x}\text{Fe}_x)_2$ . In the C14 phase, this system shows peculiar magnetic properties: In the range  $0.75 \leq x \leq 0.95$  it was reported to be an itinerant antiferromagnet, whereas for  $x > 0.95$  the magnetic susceptibility of the system, measured with a magnetic field of 1T, did not show any phase transition but very high values for a band magnet, indicating the proximity of  $\text{TaFe}_2$  to a FM instability [9]. In other words,  $\text{TaFe}_2$  is considered to be paramagnetic (PM) with strong AFM and FM spin fluctuations. This statement is supported by the chemical and electronic similarity of  $\text{TaFe}_2$  and  $\text{NbFe}_2$ , which has been investigated in our institute in detail [12-15]. By adjusting the precise composition within a narrow homogeneity range or by applying hydrostatic pressure,  $\text{NbFe}_2$  can be tuned from ferromagnetism via an intermediate spin-density-wave (SDW) modulated state to a quantum critical point (QCP). Since the atomic volume of  $\text{TaFe}_2$  is about  $13.25 \text{ \AA}^3$  and thus slightly smaller than that of  $\text{NbFe}_2$  ( $13.35 \text{ \AA}^3$ ) we expect  $\text{TaFe}_2$  to be closer to the QCP than  $\text{NbFe}_2$ .

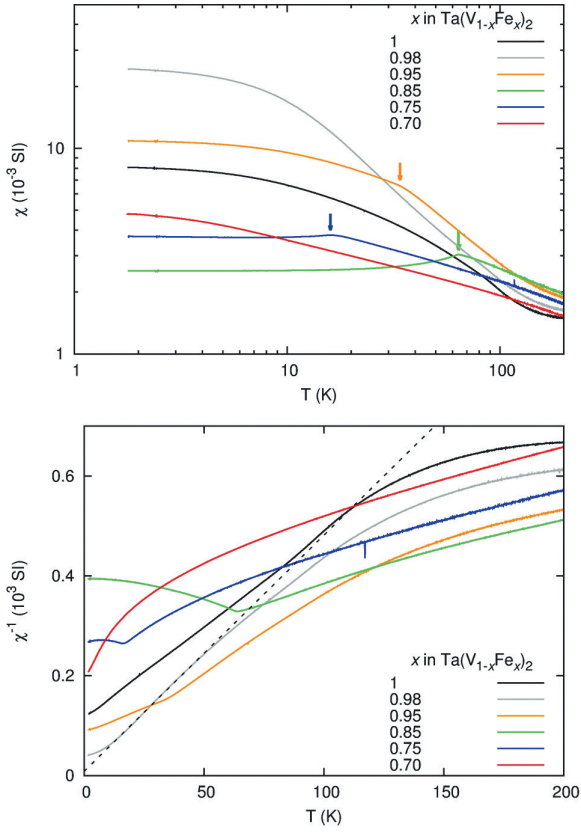


Fig. 5: Upper panel: Temperature dependence of the dc susceptibility  $\chi$  of selected samples with  $0.7 \leq x \leq 1$  taken at  $B = 1$  T. The antiferromagnetic transition temperatures  $T_N$  are indicated by arrows. Lower panel:  $\chi^{-1}$  plotted versus  $T$  to emphasize the Curie-Weiss behavior at low  $T$ : The dashed line is a linear fit to the data for the  $x = 0.983$  sample below 50 K.

To get insight into the magnetic properties of  $\text{Ta}(\text{V}_{1-x}\text{Fe}_x)_2$  we have measured the temperature ( $T$ ) and field ( $B$ ) dependencies of the magnetization ( $M$ ) of polycrystals with  $0.7 \leq x \leq 1$ . The uniform susceptibility  $\chi = M/B$  at  $B = 1$  T is plotted in Figure 5 (upper panel) for selected samples and temperatures from 300 K to 2 K: The arrows mark the peak in  $\chi$  at the Néel temperature  $T_N$ , indicating a phase transition from a PM state into a low- $T$  AFM state. At high and low V contents no phase transition is observed and the ground state is paramagnetic. However, there is a great difference between the values of the susceptibility for  $x = 0.7$  (red line) and  $x = 0.98$  (grey line) at 2 K. In the sample with  $x = 0.98$  the susceptibility is enhanced by spin fluctuations by a factor of  $\sim 240$  (Stoner factor) compared to the bare susceptibility estimated from band structure calculations. In  $\text{NbFe}_2$  this factor is  $\sim 180$  [13]. This value confirms that the

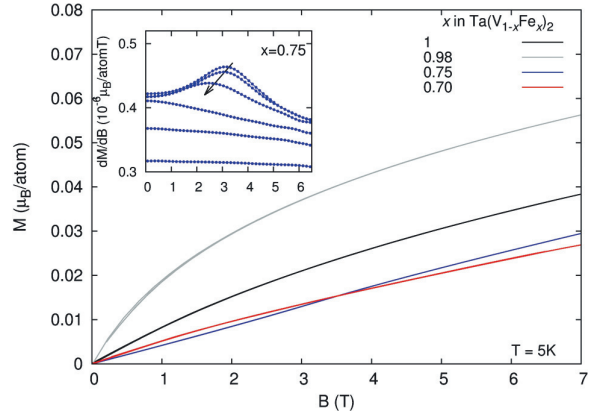


Fig. 6: Magnetization taken at 5 K of two paramagnetic samples with  $x = 1$  and 0.70, and an AFM sample with  $x = 0.75$  and  $T_N = 18$  K. Inset: Field derivative of the magnetization at different temperatures (2, 5, 10, 20, 30, 50 K) inside and outside the AFM phase for the sample with  $x = 0.75$ : The arrow indicates how the critical field which suppresses the AFM state shifts to lower values with increasing temperature.

system at  $x \sim 1$  is close to an FM instability. To know how large the fluctuating moment is in this sample, we have plotted  $\chi^{-1}$  vs  $T$  in the lower panel of Figure 5 to analyze the Curie-Weiss behavior: The dashed line is a linear fit to the data yielding a fluctuating moment of  $1.04 \mu_B$  which is much larger than the induced magnetic moment of about  $0.055 \mu_B$  measured at 7 T (see Fig. 6). This is a common property observed in all itinerant magnets.

More evidence for the presence of the AFM state is given by the field dependent magnetization shown in Figure 6 for three PM samples and one AFM sample with  $x = 0.75$ . This sample shows an inflection point around 3 T emphasized in the inset where we have plotted the derivative  $dM/dB$  vs  $B$ .  $dM/dB$  shows a clear peak which shifts to lower fields with increasing temperature, as expected for an antiferromagnet.

From our susceptibility measurements with  $B = 1$  T we have determined the magnetic phase diagram of  $\text{Ta}(\text{V}_{1-x}\text{Fe}_x)_2$  which is displayed in Figure 7. The red points indicate the Néel temperatures observed in our experiments, while the black ones have been extracted from Ref. [9], where the susceptibility has also been measured at 1 T. A clear AFM dome emerges in the PM phase of the diagram. There is a certain systematic discrepancy between these points, which is difficult to clarify. It could be explained by the fact that our V content

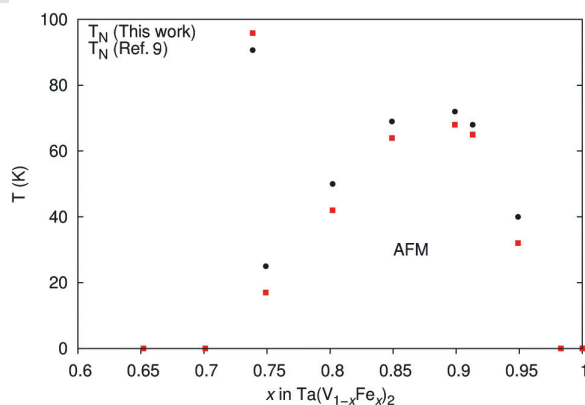


Fig. 7: Magnetic phase diagram of  $\text{Ta}(\text{V}_{1-x}\text{Fe}_x)_2$ . The red points have been extracted by dc susceptibility measurements with  $B = 1$  T, whereas the black points are taken from Ref. [9].

has been estimated by chemical analysis while the nominal one is given in Ref. [9]. However, if there is a systematic difference in  $x$ , we would expect our  $T_N$  to be higher on one side and lower on the other side of the dome maximum. The overall behavior is consistent though.

## Conclusion

The experimental determination of phase diagrams is a tedious, expensive and time consuming work because a large number of alloys have to be prepared, homogenized and characterized. Due to the ongoing improvements of theoretical methods like Density Functional Theory (DFT) and CALPHAD and due to the increasing amount of available computing power, brute force computations like the supercell approach become feasible, fast and cheap. In this work it has been shown that DFT computations in ternary Laves phases  $A(\text{B}'_{1-x}\text{B}''_x)_2$  allow to make predictions about the phase stabilities, the unit cell geometry and the site occupation factors as a function of the composition. The computed values usually exhibit an offset but can be calibrated by a small number of experimental data.

The magnetic properties of the  $\text{Ta}(\text{V}_{1-x}\text{Fe}_x)_2$  series basically agree with those found in literature and offer a great opportunity to study band-magnet quantum criticality in a stoichiometric compound at ambient pressure.

We are indebted to C. Geibel, Y. Yamada, and F. M. Grosche for useful discussions. We also thank Sergej Borisenko, who performed part of the magnetization measurements in the context of a high-school BeLL project.

## References

- [1] S. Curtarolo, D. Morgan, and G. Ceder, *CALPHAD* **29** (2005) 163.
- [2] C. C. Fischer, K. J. Tibbetts, D. Morgan, and G. Ceder, *Nature Materials* **5** (2006) 641.
- [3] J. Hafner, C. Wolverton, and G. Ceder, *MRS Bull.* **31** (2006) 659.
- [4] A. Kerkau, D. Grüner, A. Ormeci, Yu. Prots, H. Borrmann, W. Schnelle, E. Bischoff, Yu. Grin, and G. Kreiner, *Z. Anorg. Allg. Chem.* **653** (2009) 637.
- [5] G. Kresse and J. Hafner, *Phys. Rev. B* **47** (1993) 558; *ibid.* **49** (1994) 14251.
- [6] G. Kresse and D. Joubert, *Phys. Rev.* **59** (1999) 1758.
- [7] L. S. Guzei, E. M. Sokolovs, I. G. Sokolova, G. N. Ronami, and S. M. Kuznetsov, *Vestnik Moskovskogo Universiteta Seriya 2 Khimiya* **11** (1970) 696.
- [8] K. Kuo, *Act. Met.* **1** (1953) 720.
- [9] Y. Horie, S. Kawashima, Y. Yamada, G. Obara, and T. Nakamura, *J. Phys.: Conf. Ser.* **200** (2010) 032078, and references therein.
- [10] A. Ormeci, F. Chu, J. M. Willis, T. E. Mitchell, R. C. Albers, D. J. Thoma, and S. P. Chen, *Phys. Rev. B.* **54** (1996) 12753.
- [11] K. Koepernik and H. Eschrig, *Phys. Rev. B* **59** (1999) 1743.
- [12] G. Kreiner et al., “The Nature of Laves Phases” in *Scientific Report 2006-2008*, p. 126 (Max Planck Institute for Chemical Physics of Solids, Dresden, Germany 2009).
- [13] M. Brando, W. J. Duncan, D. Moroni Klementowicz, C. Albrecht, D. Grüner, R. Ballou, and F. M. Grosche, *Phys. Rev. Lett.* **101** (2008) 026401.
- [14] D. Moroni-Klementowicz, M. Brando, C. Albrecht, W. J. Duncan, F. M. Grosche, D. Grüner, and G. Kreiner, *Phys. Rev. B* **79** (2009) 224410.
- [15] D. Moroni-Klementowicz, C. Albrecht, P. G. Niklowitz, D. Grüner, M. Brando, A. Neubauer, C. Pfleiderer, N. Kikugawa, A. P. Mackenzie, and F. M. Grosche, *Phys. Status Solidi B* **247** (2010) 544.